ADVANCED FUNCTIONAL MATERIALS
www.afm-journal.de

Remarkably Improved Electrode Performance of Bulk MnS by Forming a Solid Solution with FeS – Understanding the Li Storage Mechanism

Liang Zhao, Xiqian Yu, Juezhi Yu, Yongning Zhou, Steven. N. Ehrlich, Yong-Sheng Hu, Dong Su,* Hong Li, Xiao-Qing Yang,* and Liquan Chen*

Transition metal compounds based on conversion reactions are promising electrode materials for lithium-ion batteries due to their higher lithium storage capacity compared with currently available commercial battery electrodes. Most of the studies on these materials in the literature focus on transition metal oxides and fluorides, and not much work on transition metal sulphides has been reported, partially due to their relatively poor electrochemical performance. Here, synthesis and characterization of a series of solid solution $Fe_xMn_{1-x}S$ ($x = 0.2$, 0.5, 0.8) monosulphide compounds is reported. Interestingly, hexagonal FeS and cubic MnS can form a solid solution of $Fe_xMn_{1-x}S$ ($x < 0.57$). It is demonstrated that the lithium storage voltage can be tuned by changing the Fe concentration in the $Fe_xMn_{1-x}S$ matrix; meanwhile, the discharge-charge coulombic efficiency and cycle stability of $Fe_xMn_{1-x}S$ are greatly enhanced in comparison with that of pure MnS. A half cell using $Fe_{0.5}Mn_{0.5}S$ as electrode material achieves a high first cycle coulombic efficiency of 78.0% and a high reversible capacity of ca. 477 mAh g^{-1} after 35 cycles, while for pure MnS the first cycle coulombic efficiency is only 45.9% and the capacity rapidly fades to ≈200 mAh g^{-1} after 15 cycles. Although the solid solution state of $Fe_{0.5}Mn_{0.5}S$ cannot be retained during conversion reaction as indicated by X-ray diffraction (XRD), X-ray absorption spectroscopy (XAS), and transmission electron microscopy (TEM), the initial discharge "polarization", which has been considered as one of the major hurdles for conversion reaction, can be significantly reduced by this type of material design. In addition, the size and distribution of the nucleated nanophases might also be altered by the initial solid solution state of $Fe_{0.5}Mn_{0.5}S$, contributing to the improved electrochemical performance reported here.

1. Introduction

Increasing need for electrical energy storage has promoted the great success of lithium-ion batteries (LIBs) in portable electronics, and they are also being developed for large-scale applications, such as electric vehicles and grid-scale storage. The transition from portable electronics to vehicles and grids with an expected lifetime greater than ten years will require substantial improvements of LIBs in calendar and cycling life.[1,2] In addition, vehicle applications require at least a twofold improvement of the energy and power densities. One of the promising classes of electrode materials that could meet these stringent requirements are conversion reaction based transition metal compounds (including oxides, fluorides, sulphides, and nitrides), which provide capacities several times higher than those of existing intercalation compounds, due to the multiple electron transfer per transition metal ion through conversion reaction.[3–5] Among them, transition metal oxides[6–9] and fluorides[10–15] have been intensively investigated. It was shown that Li insertion into MO/MF (M = Mn, Fe, Co, Ni, and Cu) leads to the formation of Li_2O/LiF and M nanocomposites, which are converted back to MO/MF upon Li extraction, and in some cases this conversion reaction was reported to be quite reversible.[9,15] However, not many systematic studies have been reported for sulphides, especially monosulphides, except for FeS_2, which was extensively investigated in the late 20th century for its application in commercial primary lithium-ion batteries and high temperature thermal batteries.[16,17] Some reports have shown that monosulphides suffer from poor cycling performance, limiting their use in room temperature LIBs.[18–20] Kim's research[21] reveals a general trend for the reversibility of monosulphides that follow an atomic sequence of NiS > CoS > FeS > MnS, which was suggested to result from the different electronic structure feature of the

Dr. L. Zhao, J. Z. Yu, Prof. Y.-S. Hu, Prof. H. Li, Prof. L. Q. Chen
Key Laboratory for Renewable Energy
Beijing Key Laboratory for New Energy Materials and Devices
Beijing National Laboratory for Condensed Matter Physics
Institute of Physics
Chinese Academy of Sciences
Beijing 100190, China
E-mail: yshu@aphy.iphy.ac.cn
Dr. X. Yu, Dr. Y. Zhou, Dr. S. N. Ehrlich, Dr. D. Su, Dr. X.-Q. Yang
Brookhaven National Laboratory
Upton, NY 11973, USA
E-mail: dsu@bnl.gov; xyang@bnl.gov

DOI: 10.1002/adfm.201400934

transition metal ions. Most recent work on transition metal oxides[22] and fluorides[10] considers the structure and phase evolution of the conversion reaction at atomic scale and the findings show that the electrochemical performances are highly associated with the nucleation process upon conversion. In this regard, in-depth investigation to understand the atomic structure of the sulphide compounds will enrich the knowledge of the conversion chemistry. Another aspect that impels us to reconsider monosulphides as electrode materials is the relatively low voltage hysteresis[23,24] in comparison with oxides and fluorides,[24,25] which will promote the energy conversion efficiency.

In this work, a series of the Fe-Mn binary monosulphide compound $Fe_xMn_{1-x}S$ (x = 0.2, 0.5, 0.8) has been synthesized through a solid state reaction approach, and the Li storage performance has been investigated along with pure FeS and MnS. Pure FeS exhibits a reversible capacity of more than 500 mAh g^{-1} (theoretical capacity 609 mAh g^{-1}) with a lithium insertion voltage of 1.5 V and a lithium extraction voltage of 1.8 V. MnS shows a lower lithium insertion/extraction voltage (0.9 V/1.2 V) than FeS but much poorer cycle performance. When forming the solid solution $Fe_{0.5}Mn_{0.5}S$, significant improvement of the cycle performance can be achieved compared with MnS, while a lower average lithium storage voltage is obatined compared with FeS. A variety of techniques including X-ray diffraction (XRD), X-ray absorption spectroscopy (XAS) and transmission electron microscopy (TEM), with capabilities to probe short and long range structural changes of materials, have been applied to investigate the lithium storage mechanism in binary $Fe_{0.5}Mn_{0.5}S$. The structure changes and their electrochemical behavior are discussed in detail in this work.

2. Results and Discussion

2.1. Structure and Electrochemical Performance

The morphology and crystal structure of the three as prepared compounds were characterized by scanning electron microscopy (SEM) and XRD. As shown in the SEM images of **Figure 1**, the particle size ranges from several micrometers to tens of micrometers, and the particle size becomes larger and more non-uniform as the Fe content increases. From the XRD patterns (**Figure 2**a–c), it is very interesting to find that $Fe_{0.2}Mn_{0.8}S$ and $Fe_{0.5}Mn_{0.5}S$ have the same crystal structure as MnS, but the diffraction peaks shift to higher angles with increasing the Fe content, indicating the formation of a cubic-structured $Fe_xMn_{1-x}S$ solid solution by incorporating Fe into the MnS lattice, regardless of the different crystal structures of MnS (cubic) and FeS (hexagonal). However, when the Fe content increases to $Fe_{0.8}Mn_{0.2}S$, two sets of XRD patterns relating to the hexagonal FeS phase and cubic MnS phase are discernable. The lattice parameters of this $Fe_xMn_{1-x}S$ solid solution are calculated by fitting the XRD data. The lattice parameters of $Fe_{0.2}Mn_{0.8}S$ and $Fe_{0.5}Mn_{0.5}S$ are calculated to be 5.192 Å and 5.141 Å, respectively, which are slightly lower than that of pure MnS (a = 5.222 Å). It is found that the Fe content and lattice parameter show a linear relation, as shown in Figure 2d, further proving the formation of a solid solution. It is evident that $Fe_{0.8}Mn_{0.2}S$ is a mixture of the cubic $Fe_xMn_{1-x}S$ phase and the hexagonal FeS phase. The phase ratio was determined to be 53/47 (Rietveld refinement results are shown in Figure S1, Supporting Information). By extrapolation of the line to the lattice parameter value of $Fe_xMn_{1-x}S$ in $Fe_{0.8}Mn_{0.2}S$, we can estimate that the limit of the Fe content for the solid solution is about 0.57. Therefore, the $Fe_xMn_{1-x}S$ solid solution could be formed in the range of $0 < x < 0.57$. When the x value is greater than 0.57, the product is a two-phase mixture of the $Fe_{0.57}Mn_{0.43}S$ solid solution and FeS.

Figure 3 shows the discharge-charge and capacity differential curves of the $Fe_xMn_{1-x}S$ (x = 0.2, 0.5, and 0.8) compounds for the first two cycles. It can be seen that the initial Li insertion voltage is strongly affected by the content of Fe in the $Fe_xMn_{1-x}S$ solid-solution. A single plateau located at 0.67 V and 0.86 V is observed in both $Fe_{0.2}Mn_{0.8}S$ and $Fe_{0.5}Mn_{0.5}S$, respectively, for the initial discharge process. Because the $Fe_{0.8}Mn_{0.2}S$ sample is a mixture of FeS and the $Fe_{0.57}Mn_{0.43}S$ solid solution, it is expected that the discharge plateau at 1.24 V is related to the FeS phase, while the subsequent plateau at 0.9 V is attributed to the $Fe_{0.57}Mn_{0.43}S$ solid solution. The initial charge process of $Fe_{0.2}Mn_{0.8}S$ also shows a single plateau. In the second cycle, the discharge voltage increases about 0.25 V. This type of insertion voltage difference between the first and second cycle is also observed in MnS and FeS and could originate from the large particle size of transition metal sulfides. The Li insertion and extraction voltages obtained from the capacity differential curves are 0.92 V and 1.27 V, respectively. Compared with MnS, there is no change for the lithium insertion voltage but a 50–70 mV increase in lithium extraction voltage. For $Fe_{0.5}Mn_{0.5}S$, it is interesting to note that although the initial discharge process of $Fe_{0.5}Mn_{0.5}S$ shows a single plateau, the subsequent discharge and charge processes both show two slightly-sloped plateaus. As can be seen from the capacity differential curves, the higher insertion and extraction voltages are around 1.50 V/1.83 V, which correspond to those of FeS; the lower insertion/extraction voltages are around 0.97 V/1.36 V, which are between those of MnS and FeS. For the mixed phase sample $Fe_{0.8}Mn_{0.2}S$, the high insertion/extraction voltages at 1.48 V/1.81 V are attributed to the FeS phase. The voltage peaks at 0.96 V/1.36 V, similar to those of $Fe_{0.5}Mn_{0.5}S$, are assigned to the Fe-Mn-S solid solution.

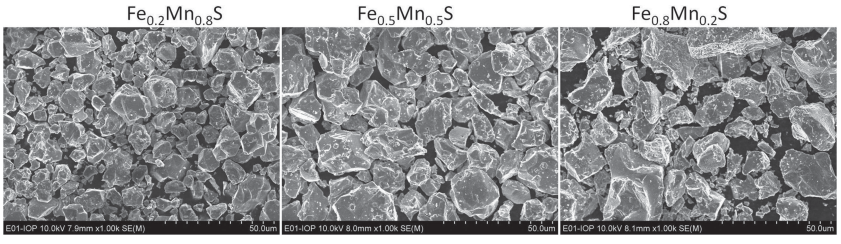

Figure 1. SEM images of the $Fe_xMn_{1-x}S$ (x = 0.2, 0.5, 0.8) samples prepared by solid state reaction.

Figure 4 shows the cycle performance of MnS, $Fe_{0.2}Mn_{0.8}S$, $Fe_{0.5}Mn_{0.5}S$, and FeS electrodes. There are few reports

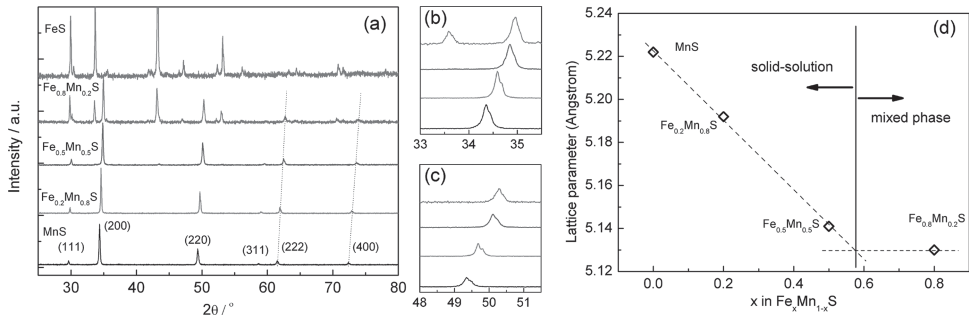

Figure 2. a) XRD patterns and d) lattice constant evolution of the $Fe_xMn_{1-x}S$ (x = 0.2, 0.5, 0.8) and MnS samples; enlarged view of the b) (200) and c) (220) reflections.

on the electrochemical performance of MnS,[18] but it is assumed that the poor cycle performance is attributed to electrode volume changes, particle cracks, and slow kinetics of the material during the conversion reaction. Our results show that MnS delivers a high capacity of 989 mAh g^{-1} for the first insertion process but with a very low initial efficiency of 45.9% (the first cycle reversible capacity is 415 mAh g^{-1}). The capacity rapidly decreased to 200 mAh g^{-1} after 15 cycles.

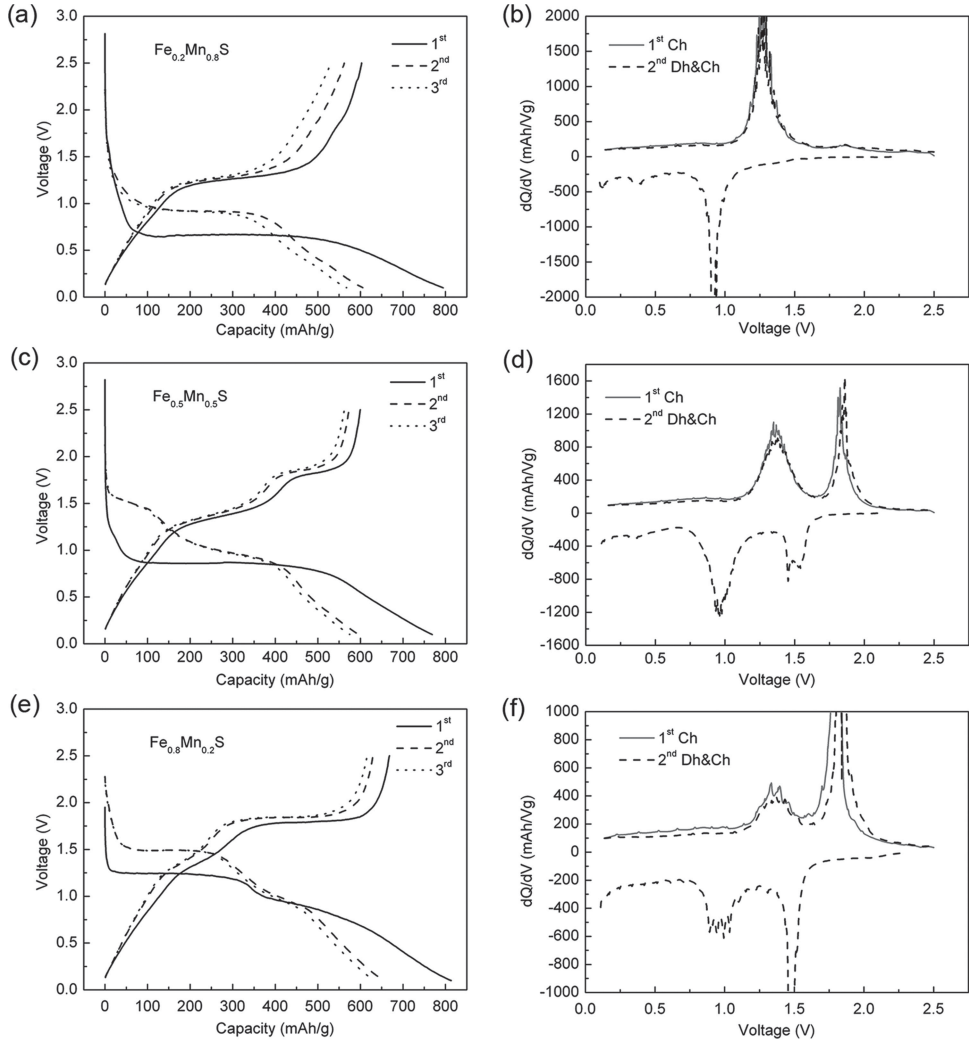

Figure 3. The first three discharge/charge curves and the first two cycles' capacity differential curves of a,b) $Fe_{0.2}Mn_{0.8}S$; c,d) $Fe_{0.5}Mn_{0.5}S$; and e,f) $Fe_{0.8}Mn_{0.2}S$ electrodes.

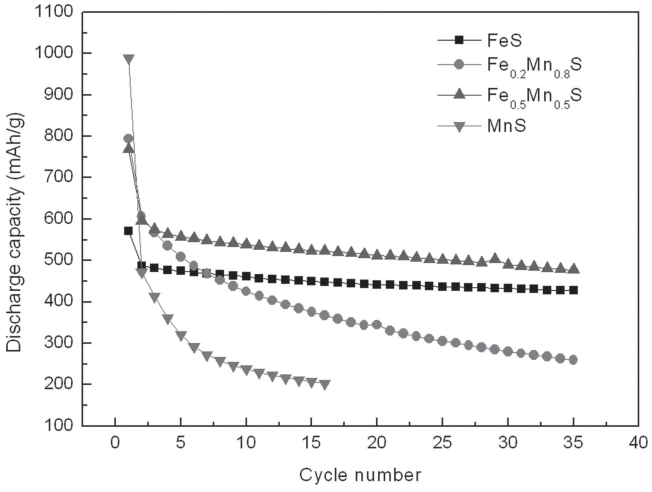

Figure 4. Cycle performance of FeS, $Fe_{0.2}Mn_{0.8}S$, $Fe_{0.5}Mn_{0.5}S$, and MnS electrodes.

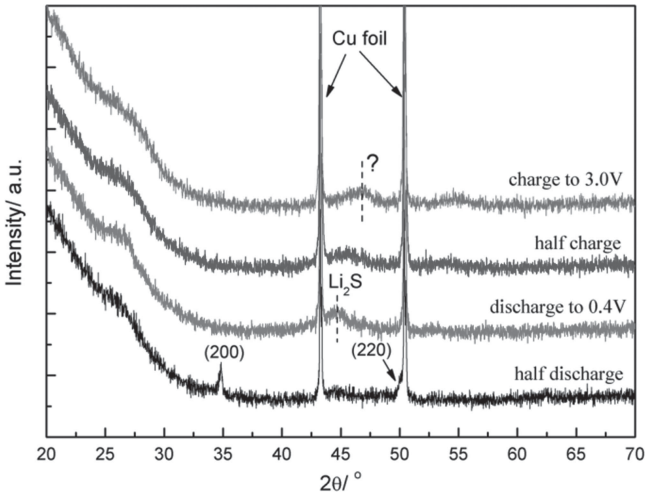

Figure 5. XRD patterns of the $Fe_{0.5}Mn_{0.5}S$ electrodes collected at different discharge and charge states.

In contrast, the FeS sample exhibits a much better cycle performance than MnS. It shows a capacity of 543 mAh g^{-1} during the first discharge process, and a reversible capacity of 427 mAh g^{-1} can be retained after 35 cycles. $Fe_{0.2}Mn_{0.8}S$ and $Fe_{0.5}Mn_{0.5}S$ show an intermediate cycle behavior between MnS and FeS. The first insertion capacity of $Fe_{0.2}Mn_{0.8}S$ and $Fe_{0.5}Mn_{0.5}S$ is 794 mAh g^{-1} and 768 mAh g^{-1} (initial couloumbic efficiency: 75.9% and 78.0%), which drops to 260 mAh g^{-1} and 477 mAh g^{-1}, respectively, after 35 cycles. This demonstrates that accommodating Fe into the MnS lattice and forming $Fe_xMn_{1-x}S$ solid solutions can greatly improve their cycle performances in comparison with pure MnS, while partially keeping the advantage of a low lithium storage voltage as found for MnS.

2.2. Reaction Mechanism

2.2.1. Ex Situ XRD Measurements

$Fe_{0.5}Mn_{0.5}S$ was chosen in order to study the reaction mechanism during Li insertion/extraction. Energy-dispersive X-ray spectroscopy (EDX) analysis was performed to further confirm the chemical composition, and the results are shown in Figure S2, Supporting Information. First, an ex situ XRD measurement was performed and the results are shown in **Figure 5**. The XRD peaks assigned to the MnS cubic phase decreased in intensity and slightly shifted to higher two-theta angles at the half-discharge state when compared with the initial state. When further discharged to 0.4 V, all XRD peaks corresponding to the original active material disappeared and a new peak representing the Li_2S phase was observed. During the re-charge process, the peaks corresponding to the original active material were not recovered. Only a broad and unidentified peak at a two-theta angle of 47° appeared while the Li_2S peak disappeared. Apparently, lithium insertion resulted in a gradual destruction of the crystal structure of $Fe_{0.5}Mn_{0.5}S$ such that its Bragg reflections disappeared and only one broad peak representing the newly formed small Li_2S grains emerged, which reversibly disappeared during the first re-charge process.

2.2.2. Ex Situ XAS Measurements

Unlike the XRD technique, which requires well crystallized samples with long range ordering, XAS is a powerful tool to characterize nanometer-sized or disordered materials. Therefore, it was used in this study for further in-depth investigations on the reaction mechanism of $Fe_{0.5}Mn_{0.5}S$ during initial lithium insertion and extraction.

In order to investigate the structure of pristine $Fe_{0.5}Mn_{0.5}S$, Fourier transformed (FT) k^2 weighted Fe and Mn K-edge extended X-ray absorption fine structure (EXAFS) spectra were collected and are shown in **Figure 6**a. The two spectra are similar within the whole measurement range, indicating similar local environments around Fe and Mn in the $Fe_{0.5}Mn_{0.5}S$ structure. The first peak at around 2.0 Å in the FT spectra corresponds to the metal-sulphur interaction in the first coordination sphere, while the second peak at around 3.2 Å originates from the metal-metal interaction in the second coordination sphere as labelled. To determine local structural parameters quantitatively, curve fitting analysis of the filtered EXAFS spectra with *R* ranging from 1.0 to 3.2 Å was performed using MnS (*Fm-3m*, cubic, rock salt structure) as the model structure. Excellent fitting results (Figure 6b) with an *R*-factor (measure of misfit between theory and data) of 0.4% were obtained. The refined bond length of the Mn-S bond, which corresponds to half of the *c* lattice parameter of the MnS phase, is 2.568 Å and this value is in excellent agreement with the value (5.14 Å = "*c*" value) obtained from X-ray diffraction. This further proves that a solid solution of the $Fe_{0.5}Mn_{0.5}S$ phase is formed with a rock salt cubic MnS structure, where Fe and Mn randomly occupy the 4a atomic site.

In order to elucidate the reaction mechanism, ex situ XAS experiments were performed. Fe and Mn K-edge XAS spectra were collected with the electrode being discharged/charged to different states (SOD/SOC) during the first discharge/charge cycle as marked on the discharge/charge curve. Corresponding X-ray absorption near edge structure (XANES) spectra are displayed in **Figure 7**a. It is surprising to find that the reduction of Fe and Mn does not take place simultaneously although

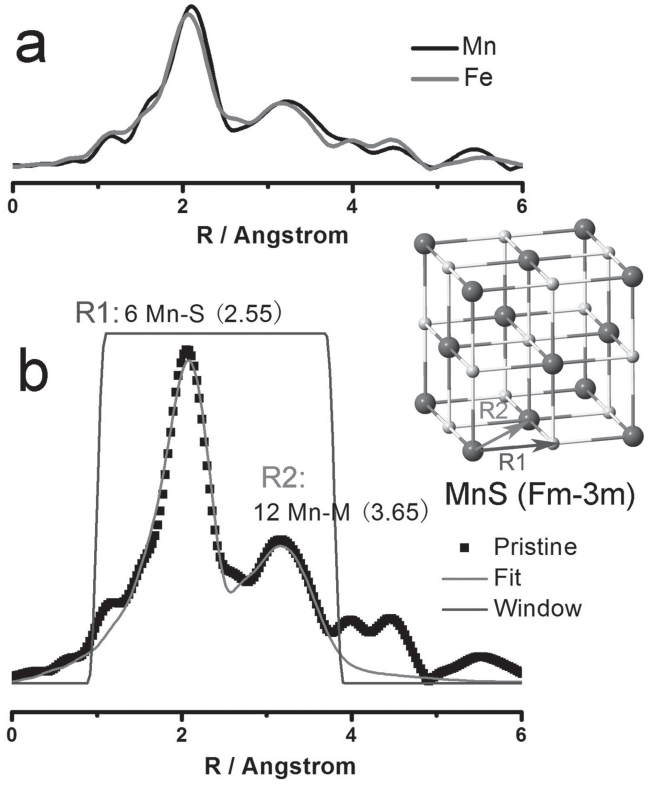

Figure 6. a) Comparison of the magnitude of Fourier transformed k^2-weighted Mn and Fe K-edge EXAFS spectra; b) experimental (■) and fitted (–) magnitude of the Fourier transformed k^2-weighted Mn K-edge EXAFS spectrum for the pristine $Fe_{0.5}Mn_{0.5}S$ powder (Δk = 3.0–11.5 Å^{-1}, fitting R range = 1.0 –3.2 Å). Inset figure: Structure of $Fe_{0.5}Mn_{0.5}S$ (*Fd-3m*, cubic, rock-salt structure)

the voltage profile appears as a single flat plateau. The most visible changes for Fe take place in the early stage up to the middle part of the discharge process (state a, b, and c), while for Mn the most obvious changes start from the middle part and continue to the end of the discharge process. For both Mn and Fe, the shape of the XANES spectra changes but no rigid edge shift is observed. An isosbestic point[26] can be observed in the case of FeF_2 suggesting that only two species (FeF_2 and Fe) exist with changing concentration ratios in the mixture during the reaction. However, a closer inspection of the spectra collected on the $Fe_{0.5}Mn_{0.5}S$ electrodes reveals that not all XANES spectra intersect exactly at one point. The "unfocused" isosbestic point presented here indicates that the initial discharge process of $Fe_{0.5}Mn_{0.5}S$ does not follow a simple reaction of $Li + Fe_{0.5}Mn_{0.5}S \rightarrow Fe + Mn + Li_2S$. This agrees well with the asynchronized reaction of Fe and Mn aforementioned. During the first charging, the spectra basically change back towards the original state for both Fe and Mn. It can be seen that the re-conversion reaction of Mn takes place first followed by Fe, which is in good agreement with the observation of two well-separated voltage plateaus on the charge curve.

Linear combination (LC) fitting[26] of XANES spectra was performed to determine the ratio of the converted phase (i.e., metallic Fe and Mn). Thereby, the valence states of Fe and Mn of the electrode at each state can be quantitatively determined and the results are shown in Figure 7b. The reaction sequence of Mn and Fe can be directly observed. In addition, the reversibility of the conversion reaction can also be estimated. The average oxidation states of Mn and Fe are estimated to be 1.63 and 1.08, respectively, at the fully charged (state "l" at 3 V) electrode, indicating that 81.5% of metallic Mn and 54% of metallic Fe have been reconverted and oxidized back to Mn^{2+} and Fe^{2+}, which corresponds to a capacity of 250 mAh g^{-1} and 166 mAh g^{-1}, respectively. The total capacity delivered from the oxidation of Fe and Mn is 416 mAh g^{-1}, smaller than the experimentally recorded charge capacity of 600 mAh g^{-1}. The extra capacity obtained beyond the oxidation of Fe and Mn might be attributed to either the reversible interfacial charge or other mechanisms (e.g., reversible SEI formation/decomposition).[27–30] It is also noteworthy that the extra capacity is mainly delivered upon the early stage of the charging process (sloping region, 0.25–1.2 V), where Fe and Mn show only a slight oxidation.

EXAFS analysis was performed to investigate the local structural changes of $Fe_{0.5}Mn_{0.5}S$ for further understanding the conversion reaction. Figure 7c shows the magnitude of Fourier transformed (FT) k^2-weighted Mn and Fe K-edge EXAFS spectra for the $Fe_{0.5}Mn_{0.5}S$ electrode at different SODs/SOCs. During the first discharging, the general features for both Mn and Fe are the decreasing intensities of the two peaks representing Mn/Fe-S (≈2.1 Å) and Mn/Fe-metal (≈3.4 Å) bonds in the $Fe_{0.5}Mn_{0.5}S$ structure, accompanied by an increasing intensity of new peaks located at ≈2.0 Å and ≈2.2 Å for Mn and Fe, respectively, with increasing the discharge state. The decreasing intensities of the Mn/Fe-S and Mn/Fe-M peaks indicate the cleavage of the $Fe_{0.5}Mn_{0.5}S$ framework upon lithiation. The newly emerging peaks can be assigned to the first metal-metal coordination shell of the metallic Fe and Mn phase formed through the conversion reaction. Therefore, the EXAFS results clearly support the conversion reaction proposed in equation (1) described later in this paper, suggesting that the reduction of Fe^{2+} takes place first followed by the reduction of Mn^{2+}. In addition, a continuous shift of the Mn-S bond length to lower values can be observed in the early stage of the discharge process (Figure 7, state a–d). This is in good agreement with XRD showing a peak shift during discharging, and also confirms that the initial lithiation does not proceed as a simple two-phase reaction. During the first charging, the most visible changes are the increased intensities of the peaks located at 2.1 Å at state h, i, j for Mn and state j, k, l for Fe, corresponding to the voltage plateaus of ≈1.4 V and ≈1.8 V, respectively. These results are also in good agreement with XANES.

Due to the overlap of the Mn/Fe-S (for $Fe_{0.5}Mn_{0.5}S$) and metal-metal (for metallic Fe/Mn phases) bond, semi-quantitative analyses were performed only on the fully discharged (state "g") and fully charged (state "l") samples, where metallic Fe/Mn is the major phase at state "g" and reconverted FeS/MnS is the major phase at state "l". **Figure 8** shows a comparison of the FT spectra at the discharged state (state "g" at 0.25 V) and the reference Mn and Fe foil (bulk properties). The amplitude of the peaks for both Mn and Fe at the discharged state are smaller than that for Mn and Fe foil. This intensity reduction is predominantly caused by the decrease of the coordination number resulting from the increased ratio of surface to bulk atoms in the particles. This effect is more pronounced when

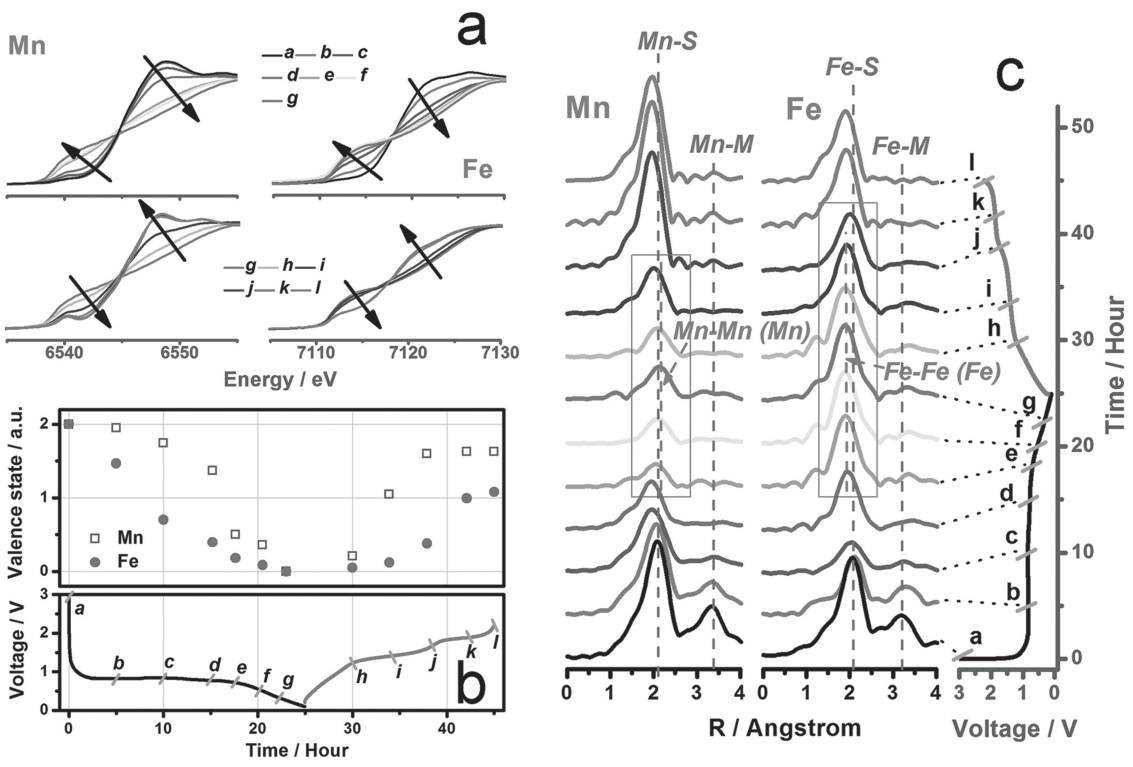

Figure 7. a) XANES and c) magnitude of Fourier transformed k^2-weighted EXAFS spectra (in a k-range from ≈3.0–11.5 Å^{-1}) of Mn and Fe; b) average valence state of Fe (/Mn) estimated from linear combination fitting of the Fe (/Mn) ratio in corresponding electrodes discharged/charged at different SODs/SOCs (labelled schematically on the voltage profile curve).

the particle size decreases down to the nanometer range.[13,31] Therefore, both converted metallic Fe and Mn are proposed to nucleate in the form of nanometer-sized particles which are dispersed in the matrix of Li_2S. As shown in Figure 8a for Mn, the major features of the spectrum for converted Mn are similar to that for Mn foil with peaks located at ≈2.2, 3.5, and 4.8 Å, which indicates that the nanometer-sized metallic Mn phase formed through the conversion reaction could mainly preserve the structure of the α-Mn phase. In contrast, the FT amplitude difference between converted Fe in $Fe_{0.5}Mn_{0.5}S$ and Fe foil is much larger. The position of the FT peaks is not exactly the same as for the reference Fe foil, which shows typical features of body centred cubic (bcc) Fe. These results indicate that the converted Fe formed in the Li_2S matrix might be much smaller in particle size and/or more disordered in structure than the converted Mn and shows a structure deviation from the ideal α-Fe phase (bcc structure). Furthermore, the nucleation behaviour of the metallic phase is found to be different in different conversion type compounds, which will be discussed in detail elsewhere. We believe that this will allow to determine the electrochemical behaviour of the conversion reaction.

For the fully charged state (**Figure 9**, state l: 3 V), the Fe and Mn nanoparticles are consumed and poorly crystallized phases are formed. Only the first FT peak can be seen while the peak features at longer distances are attenuated, suggesting a reduction in crystallinity and/or particle size. The first FT peak located at ≈1.8 Å arises at a shorter distance in comparison with that of crystallized pristine $Fe_{0.5}Mn_{0.5}S$. This agrees well with the XRD results and can be explained by the compressive tension resulting from the substantial surface tension of nanometer-sized particles of high radius, which drives the atomic positions of the surface atoms to shift away from ideal sites towards the nanoparticle's core.[32] Both the phase and morphology changes after the conversion and reconversion reaction will be further identified by TEM, which will be described in the following.

2.2.3. TEM Observations

Figure 10 shows annular dark-field scanning transmission electron microscopy (ADF-STEM) images from the pristine, discharged (lithiated, 0.4 V) and charged (delithiated, 3 V) $Fe_{0.5}Mn_{0.5}S$ samples. Mn $L_{2,3}$ edges (640 and 652 eV) and Fe $L_{2,3}$ edges (708 and 721 eV) are used for probing the local elemental distribution. Figure 10d–f shows scanning transmission electron microscope elemental mapping by electron energy-loss spectroscopy (STEM-EELS) on the selected areas marked in Figures 10a–c. The pristine sample has a uniform contrast in the ADF image, which indicates a homogeneous distribution of Fe and Mn, in good agreement with the XRD and XAS observations. After being lithiated, significant morphology changes can be observed, with Fe nanoparticles in the size of ≈3–5 nm (Figure 10b) being formed, as evidenced by EELS mapping in Figure 10e. The morphology of lithiated $Fe_{0.5}Mn_{0.5}S$ appears to consist of nanometer-sized Fe and Mn immersed within a Li_2S matrix. Interestingly, after being delithiated (Figure 10c,f), a porous morphology is observed in the ADF image and Mn-rich regions are observed by EELS mapping.[33] Phase segregation

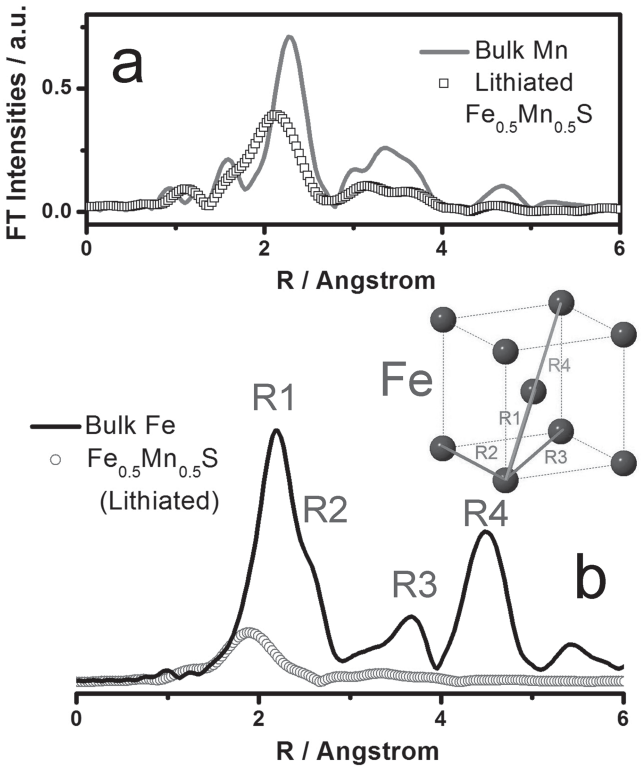

Figure 8. Comparison of the magnitude of Fourier transformed a) Mn and b) Fe K-edge spectra of the $Fe_{0.5}Mn_{0.5}S$ sample collected at the fully discharged state (0.25 V) and Mn and Fe foil, respectively.

of Fe, Mn, and Li_2S provides further evidence for the asynchronous conversion and formation of Fe and Mn nanophases during initial discharging, as revealed by the XAS analysis. The reconversion (charge) process proceeds locally, due to the Li^+ transport properties within these nanocomposites[34] (here Li_2S/Fe/Mn). Therefore, Mn and Fe phase separation is expected to occur in the subsequent cycles, as reflected directly by the well-separated voltage plateaus on the charge/discharge curve.

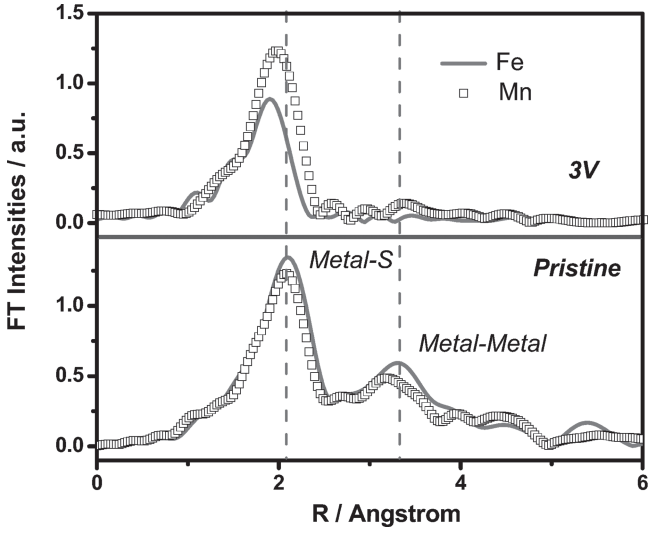

Figure 9. Comparison of the magnitude of Fourier transformed Mn and Fe K-edge EXAFS spectra for pristine and charged (3 V) electrodes.

The phases of these samples are further indentified by selected area electron diffraction (SAED) patterns. The SAED pattern of the pristine sample (**Figure 11**a) matches well with a single MnS-cubic phase. For the lithiated sample (Figure 11b), a cubic Li_2S phase and a distorted Fe phase can be identified along with an Al phase as an internal standard. It is interesting to note that the reflections of the Fe particles exhibit a nonlinear expansion, suggesting that the nucleated Fe nanoparticles derive from the room temperature stabilized bcc structure, in agreement with the EXAFS results. The average lattice constant compared with that of bulk bcc Fe expands by about 8%. The delithiated sample (Figure 11c) contains a cubic major phase and a hexagonal minor phase. Considering the STEM-EELS mapping results shown in Figure 10f, we can attribute the cubic phase to MnS and the hexagonal phase to FeS. High-resolution transmission electron microscopy (HRTEM) images of the pristine, lithiated, and delithiated samples are shown in Figures 11d–f, where the features of local atom rearrangement during the lithiation are compared. A high density of defect structures was observed in the pristine sample, which probably results from the large strain due to the structural difference between cubic MnS and hexagonal FeS. Nanograins of ≈3–5 nm were observed in lithiated and delithiated samples. Fast Fourier transform (FFT) patterns clearly show that these nanograins have a similar crystal orientation, as recently observed in nanometer-sized Fe converted from FeF_2, where a unique crystallographic orientation of the resultant Fe relative to the original FeF_2 host has been revealed.[34]

On the basis of the XRD, XAS, and TEM observations, the conversion reaction mechanism of $Fe_{0.5}Mn_{0.5}S$ can be proposed as follows:

(1) Reaction during the initial discharge process:

$$2x\mathrm{Li} + \mathrm{Fe_{0.5}Mn_{0.5}S} \rightarrow x\mathrm{Fe} + \mathrm{Fe_{0.5-x}Mn_{0.5}S_{1-x}} + x\mathrm{Li_2S}\ (x \le 0.5)$$

$$2(1-x)\mathrm{Li} + \mathrm{Fe_{0.5-x}Mn_{0.5}S_{1-x}} \rightarrow (0.5-x)\mathrm{Fe} + 0.5\mathrm{Mn} + 2(1-x)\mathrm{Li_2S}$$

(2) Reaction during the initial charge process:

$$\mathrm{Li_2S} + \mathrm{Mn} \rightarrow \mathrm{MnS} + 2\mathrm{Li}\ (\approx 1.4\ \mathrm{V\ vs.\ Li^+/Li})$$

$$\mathrm{Li_2S} + \mathrm{Fe} \rightarrow \mathrm{FeS} + 2\mathrm{Li}\ (\approx 1.8\ \mathrm{V\ vs.\ Li^+/Li})$$

2.3. Discussion

Although many questions regarding the detailed mechanisms of the conversion reaction still remain unanswered, our results may shed some light on several key issues of the conversion reaction:

(1) Reversibility and cyclability: Kim's previous research[21] revealed that the reversibility of the conversion reaction for transition metal monosulphides increases in the atomic sequence NiS > CoS > FeS > MnS, which is further confirmed in our

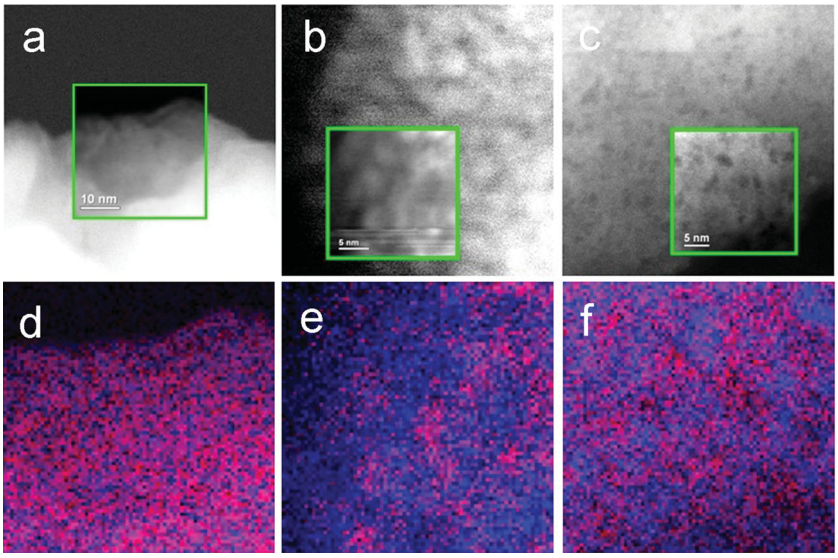

Figure 10. a–c) Representative STEM images of pristine, discharged (0.4 V), and charged (3 V) samples, respectively. d–f) Relative distribution of Fe (red) and Mn (blue), retrieved from their $L_{2,3}$ edges from the square regions of (a–c), respectively. The spatial resolutions (steps) of d, e, and f are 4.1, 3.0, and 3.0 Å, respectively.

binary FeS-MnS system. Our results show that the crystallinity and size of the nucleated nanophases might be different for Fe and Mn during the conversion reaction of $Fe_{0.5}Mn_{0.5}S$, indicating that the size and distribution of the nanometer-sized new phases may directly impact the reversibility and cyclability of the conversion reaction based electrode materials. On the other hand, lattice distortion and unique crystallographic orientation behaviour of the nucleated metallic nanophase, as also reported in recent studies on Fe_2O_3[22] and FeF_2,[34] suggest that the nucleation process might be determined by the structure and intrinsic mechanical properties of the transition metal compounds. Therefore, modification of pristine materials, such as demonstrated in this paper, by incorporating Fe into MnS to form a solid solution phase, could provide a new approach to improve the electrochemical performance.

(2) Initial discharge polarization: The experimental conversion reaction potential (discharge voltage) is always lower than the emf. (electromotive force) estimated from the Nernst equation.[4] The difference, named "polarization", is a general feature for the conversion reaction and is always large for the initial discharge process (≥0.5 V). Therefore, some thermodynamically feasible compounds cannot be converted through electrochemical conversion reaction due to the large polarization, such as rutile TiO_2 (emf. 0.608 V vs. Li^+/Li).[4] Our observations on $Fe_xMn_{1-x}S$ solid-solution materials indicate that the initial conversion reaction polarization can be tuned for $Fe_{0.5}Mn_{0.5}S$, as schematically shown in Figure S3, Supporting Information. The reaction polarization for $Fe_{0.5}Mn_{0.5}S$ in the Mn conversion reaction region has been reduced in comparison with that for pure MnS. This strategy might be suitable to be applied to other conversion reaction typed compounds to reduce the initial conversion reaction polarization.

(3) Voltage hysteresis: Voltage hysteresis will lower the energy storage efficiency. It is observed in all conversion type materials and cannot be eliminated by slow-rate charging/discharging.[23] From a thermodynamic point of view, strain and interfacial energy have been assumed to cause hysteresis.[35,36] Our experimental results confirm that strain exists within the nanocomposites ($Fe/Mn/Li_2S$) formed during conversion reaction, as evidenced by the observation of distorted and coherent nucleated metallic nanoparticles. A similar phenomenon has been observed in the cases of Fe_2O_3[22] and FeF_2,[32] where nanometer-sized Fe with different extension of distortion were formed, respectively. This is expected to result in a difference in voltage hysteresis. Experimentally, there is a general trend that transition metal monosulphides show lower voltage hysteresis than transition metal oxides, while transition metal fluorides exhibit the largest voltage hysteresis.[10] On this aspect, transition metal monosulphides could be the best candidate as conversion type anode materials among all transition metal compounds for lithium-ion batteries.

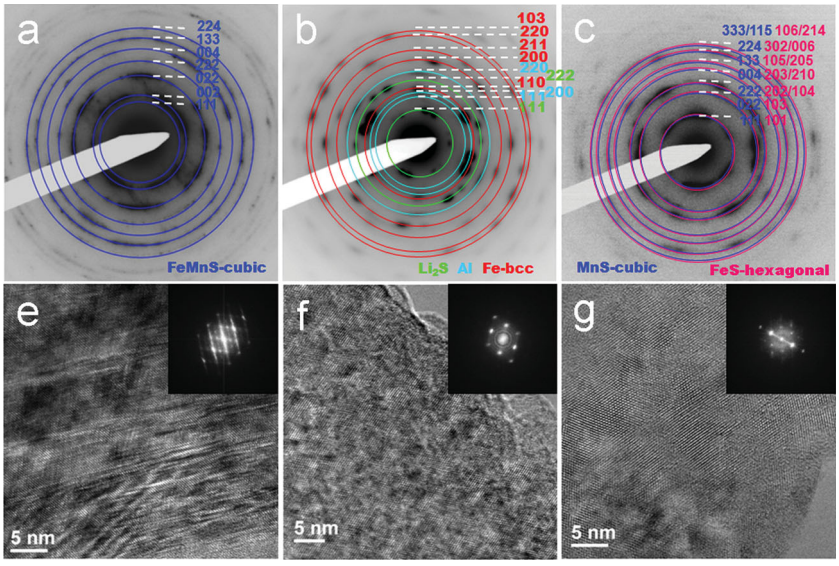

Figure 11. a–c) SAED patterns of the pristine, discharged (0.4 V), and charged (3 V) samples, respectively. The reflections for each structure are marked with circles and the name of the phase is listed under the respective pattern. d–f) High resolution TEM images of the samples shown in (a–c). The insets are FFTs of these images.

3. Conclusions

A series of $Fe_xMn_{1-x}S$ (x = 0.2, 0.5, 0.8) monosulphide compounds was synthesized through a simple solid state reaction method.

It is demonstrated that two transition metal sulphides, FeS and MnS, with different crystal structures can form a solid solution. The average lithium storage voltage increases with the increase of the Fe content in $Fe_xMn_{1-x}S$ electrodes. Comparing these compounds with pure MnS, the electrochemical performance of the $Fe_xMn_{1-x}S$ electrodes is greatly enhanced in terms of discharge-charge coulombic efficiency and cycle stability. $Fe_{0.5}Mn_{0.5}S$ exhibits a high coulombic efficiency of 78.0% for the first cycle and a high reversible capacity of ca. 477 mAh g^{-1} after 35 cycles, while for pure MnS the coulombic efficiency is only 45.9% for the first cycle and the capacity rapidly fades to ≈200 mAh g^{-1} after 15 cycles. Combination of XRD, XAS, and TEM measurements reveals that the solid solution state of $Fe_{0.5}Mn_{0.5}S$ is destroyed during initial lithiation, and the conversion reaction involving FeS and MnS proceeds separately in the subsequent cycles. Although the initial solid solution state cannot be preserved during conversion reaction, the large first discharge "polarization", which has been considered as one of the major hurdles of the conversion reaction, can be significantly reduced by incorporating two compounds with different Li insertion/extraction potential into a solid solution. This strategy might also be applied to other energy storage systems, e.g. metal fluorides, when designing materials with suitable operating voltage and good cycle performance. On the other hand, size and distribution of the nucleated nanometer-sized phases, adjusted and altered by the initial solid solution nature of $Fe_{0.5}Mn_{0.5}S$, are shown to be critical for the electrochemical performance of these conversion type materials.

4. Experimental Section

4.1. Material Synthesis and Characterization

All the samples were prepared using a solid state reaction method. For FeS, MnS, and $Fe_xMn_{1-x}S$ (x = 0.2, 0.5, 0.8), the Fe and/or Mn powder and S powder were carefully ground and pressed into tablets. Then the tablets were sealed into vacuum quartz tubes and heat-treated at 900 °C for 40 h. After cooling down to room temperature, the obtained samples were ground for electrode preparation. The morphologies of the samples were observed using a SEM (Hitachi S-4800). The structure of the samples was characterized with a X'Pert Pro MPD X-ray diffractometer (Philips, Holland) using Cu-Kα radiation (1.5405 Å), and the exact lattice parameters were obtained by refining the XRD data using Fullprof.

4.2. Electrochemistry Test

The working electrode was prepared by spreading a slurry of the active materials (70 wt%), acetylene black (20 wt%), and sodium alginate binder (10 wt%) on a Cu foil with distilled water as the solvent.[37,38] The electrode was dried at 100 °C in vacuum for 10 h before use. The coin cells were assembled with pure lithium foil as the counter electrode and a glass fiber as the separator in an argon-filled glove box. The electrolyte was 1.2 M $LiPF_6$ in ethylene carbonate (EC) and dimethyl carbonate (DMC) as solvent (3:7 by volume, Novolyte Inc.). The charge/discharge measurements were carried out on a Land BT2000 battery test system (Wuhan, China) at a current rate of 0.1 C (1 C = 600 mA g^{-1}) at room temperature. The MnS and $Fe_xMn_{1-x}S$ (x = 0.2, 0.5, 0.8) electrodes were discharged and charged in the voltage range of 0.1–2.5 V. The voltage range for the FeS electrode was 1.0–2.5 V. The cycle performance of the FeS electrode between 0.1 and 2.5 V is shown in Figure S4, Supporting Information.

4.3. X-Ray Absorption Spectroscopy

Samples for XAS experiments were ex situ prepared. The electrodes were discharged/charged to different states of discharge/charge (SOD/SOC) with a current density of 30 mA g^{-1} (corresponding to 0.05 C) at room temperature. Mn and Fe K-edge XAS spectra were collected in the transmission mode at beamlines X18A and X19A at the National Synchrotron Light Source (NSLS, BNL), using a Si (111) double-crystal monochromator detuned to 35–45% of its original maximum intensity to eliminate the high order harmonics. A reference spectrum of each element was simultaneously collected with the corresponding transition metal foil. Energy calibration was carried out using the first inflection point of the K-edge spectrum of the transition metal foil as reference (i.e., Mn: 6539 eV).[39] The EXAFS data were analyzed using the Athena and Artemis programs.

4.4. Transmission Electron Microscopy Experiments

TEM samples were prepared by scratching samples from the electrode onto a Holey Carbon 400 mesh Cu grid (Ted Pella, Inc.). HRTEM and SAED were obtained using a JEOL TEM equipped with a Schottky field-emission gun (FEG), with Cs = 1.0 mm operated at 200 kV. The local elemental distributions were characterized by the STEM-EELS method using a Cs-corrected Hitachi HD-2700C equipped with a Cold-FEG, operated at 200 kV.[40] Images were acquired using a probe convergence semiangle of 27 mrad, while the inner collection angle of the ADF detector was 64 mrad. The EELS data were collected using an Engina ER (Gatan) detector, with a collection half-angle of 26 mrad. The energy resolution was about 1.3 eV at the dispersion of 1.25 eV/ch. At a probe size of 1.3 Å, the beam current (≈30–40 pA), dwelling time (about 0.01 S) and steps (≈3–5 Å) were carefully selected to avoid electron-beam damage.[41]

Supporting Information

Supporting Information is available from the Wiley Online Library or from the author.

Acknowledgements

L.Z. and X.Y. contributed equally to this work. Y.-S.H. designed this work; L.Z. and J.Z.Y. carried out the synthesis and electrochemical experiments; L.Z. and X.Yu carried out the ex situ XRD experiments and data analysis; X.Y. performed the XAS experiments and data analysis with X.-Q.Y.; X.Y. and D.S. carried out the TEM experiments and data analysis; X.Y., L.Z., D.S., and Y.-S.H. wrote the paper; all the authors participated in the analysis of the experimental data and discussions of the results. This work was supported by funding from the "973" Projects (2010CB833102, 2012CB932900), NSFC (51222210, 11234013), "Strategic Priority Research Program" of the Chinese Academy of Sciences (Grant No. XDA01020304) and One Hundred Talent Project of the Chinese Academy of Sciences. The work at Brookhaven National Laboratory was supported by the U. S. Department of Energy, the Assistant Secretary for Energy Efficiency and Renewable Energy, Office of Vehicle Technologies under Contract Number DEAC02–98CH10886. The authors acknowledge the technical support from beamline scientists at beamline X18A and X19A at NSLS (BNL) and Center for Functional Nanomaterials (CFN, BNL).

Received: March 22, 2014
Revised: April 12, 2014
Published online: July 14, 2014

[1] B. Dunn, H. Kamath, J. M. Tarascon, *Science* **2011**, *334*, 928.
[2] L. M. Suo, Y.-S. Hu, H. Li, M. Armand, L. Q. Chen, *Nat. Commun.* **2013**, *4*, 1481.
[3] P. Poizot, S. Laruelle, S. Grugeon, L. Dupont, J.-M. Tarascon, *Nature* **2000**, *407*, 496.
[4] H. Li, P. Balaya, J. Maier, *J. Electrochem. Soc.* **2004**, *151*, A1878.
[5] J. Cabana, L. Monconduit, D. Larcher, M. R. Palacin, *Adv. Mater.* **2010**, *22*, E170.
[6] B. Wang, J. S. Chen, H. B. Wu, Z. Wang, X. W. Lou, *J. Am. Chem. Soc.* **2011**, *133*, 17146.
[7] X. Fang, X. Lu, X. Guo, Y. Mao, Y.-S. Hu, J. Wang, Z. Wang, F. Wu, H. Liu, L. Chen, *Electrochem. Commun.* **2010**, *12*, 1520.
[8] W. M. Zhang, X. L. Wu, J. S. Hu, Y. G. Guo, L. J. Wan, *Adv. Funct. Mater.* **2008**, *18*, 394.
[9] L. J. Zhi, Y. S. Hu, B. El Hamaoui, X. Wang, I. Lieberwirth, U. Kolb, J. Maier, K. Mullen, *Adv. Mater.* **2008**, *20*, 1727.
[10] F. Badway, N. Pereira, F. Cosandey, G. G. Amatucci, *J. Electrochem. Soc.* **2003**, *150*, A1209.
[11] F. Wang, R. Robert, N. A. Chernova, N. Pereira, F. Omenya, F. Badway, X. Hua, M. Ruotolo, R. Zhang, L. J. Wu, V. Volkov, D. Su, B. Key, M. S. Whittingham, C. P. Grey, G. G. Amatucci, Y. M. Zhu, J. Graetz, *J. Am. Chem. Soc.* **2011**, *133*, 18828.
[12] Y. Ma, S. H. Garofalini, *J. Am. Chem. Soc.* **2012**,*134*, 8205.
[13] K. M. Wiaderek, O. J. Borkiewicz, E. C. Martínez, R. Robert, N. Pereira, G. G. Amatucci, C. P. Grey, P. J. Chupas, K. W. Chapman, *J. Am. Chem. Soc.* **2013**, *135*, 4070.
[14] W. Zhang, P. N. Duchesne, Z. L. Gong, S. Q. Wu, L. Ma, Z. Jiang, S. Zhang, P. Zhang, J. X. Mi, Y. Yang, *J. Phys. Chem. C* **2013**, *117*, 11498.
[15] S. W. Kim, D. H. Seo, H. Gwon, J. Kim, K. Kang, *Adv. Mater.* **2010**, *22*, 5260.
[16] H. Siyu, L. Xinyu, L. QingYu, C. Jun, *J. Alloys Compd.* **2009**, *472*, L9.
[17] T. D. Kaun, P. A. Nelson, L. Redey, D. R. Vissers, G. L. Henriksen, *Electrochim. Acta* **1993**, *38*, 1269.
[18] N. Zhang, R. Yi, Z. Wang, R. R. Shi, H. D. Wang, G. Z. Qiu, X. H. Liu, *Mater. Chem. Phys.* **2008**, *111*, 13.
[19] S. H. Kim, Y. J. Choi, D. H. Kim, S. H. Jung, K. W. Kim, H. J. Ahn, J. H. Ahn, H. B. Gu, *Surf. Rev. Lett.* **2008**, *15*, 35.
[20] J. L. Gomez-Camer, F. Martin, J. Morales, L. Sanchez, *J. Electrochem. Soc.* **2008**, *155*, A189.
[21] Y. Kim, J. B. Goodenough, *J. Phys. Chem. C* **2008**, *112*, 15060.
[22] B. Shyam, K. W. Chapman, M. Balasubramanian, R. J. Klingler, G. Srajer, P. J. Chupas, *Angew. Chem. Int. Ed.* **2012**, *51*, 4852.
[23] P. L. Taberna, S. Mitra, P. Poizot, P. Simon, J. M. Tarascon, *Nat. Mater.* **2006**, *5*, 567.
[24] J. P. Sun, K. Tang, X. Q. Yu, J. Hu, H. Li, X. J. Huang, *Solid State Ionics* **2008**, *179*, 2390.
[25] X. Q. Yu, Y. He, J. P. Sun, K. Tang, H. Li, L. Q. Chen, X. J. Huang, *Electrochem. Commun.* **2009**, *11*, 791.
[26] X. Yu, Q. Wang, Y. N. Zhou, H. Li, X.-Q. Yang, K.-W. Nam, S. N. Ehrlich, S. Khalid, Y. S. Meng, *Chem. Commun.* **2012**, *48*, 11537.
[27] a) H. Li, G. Richter, J. Maier, *Adv. Mater.* **2003**, *15*, 736; b) P. Balaya, H. Li, L. Kienle, J. Maier, *Adv. Funct. Mater.* **2004**, *13*, 621.
[28] Y. F. Zhukovskii, P. Balaya, E. A. Kotomin, J. Maier, *Phys. Rev. Lett.* **2006**, *96*, 058302.
[29] X. Q. Yu, J. P. Sun, K. Tang, H. Li, X. J. Huang, L. Dupont, J. Maier, *Phys. Chem. Chem. Phys.* **2009**, *11*, 9497.
[30] Y.-Y. Hu, Z. Liu, K.-W. Nam, O. J. Borkiewicz, J. Cheng, X. Hua, M. T. Dunstan, X. Yu, K. M. Wiaderek, L.-S. Du, K. W. Chapman, P. J. Chupas, X.-Q. Yang, C. P. Grey, *Nat. Mater.* **2013**, *12*, 1130.
[31] S. Calvin, M. M. Miller, R. Goswami, S. F. Cheng, S. P. Mulvaney, L. J. Whitman, V. G. Harris, *J. Appl. Phys.* **2003**, *94*, 778.
[32] J. S. Vermaak, C. W. Mays, D. K. Wilsdorf, *Surf. Sci.* **1968**, *12*, 128.
[33] Y.-S. Hu, Y.-G. Guo, W. Sigle, S. Hore, P. Balaya, J. Maier, *Nat. Mater.* **2006**, *5*, 713.
[34] F. Wang, H. C. Yu, M. H. Chen, L. J. Wu, N. Pereira, K. Thornton, A. V. Ven, Y. M. Zhu, G. G. Amatucci, J. Graetz, *Nat. Commun.* **2012**, *3*, 1201.
[35] O. Delmer, P. Balaya, L. Kienle, J. Maier, *Adv. Mater.* **2008**, *20*, 501.
[36] O. Delmer, J. Maier, *Phys. Chem. Chem. Phys.* **2009**, *11*, 6424.
[37] I. Kovalenko, B. Zdyrko, A. Magasinski, B. Hertzberg, Z. Milicev, R. Burtovyy, I. Luzinov, G. Yushin, *Science* **2011**, *333*, 75.
[38] a) Y. Sun, L. Zhao, H. L. Pan, X. Lu, L. Gu, Y.-S. Hu, H. Li, M. Armand, Y. Ikuhara, L. Q. Chen, X. J. Huang, *Nat. Commun.* **2013**, *4*, 1870; b) H. L. Pan, X. Lu, X. Q. Yu, Y.-S. Hu, H. Li, X. Q. Yang, L. Q. Chen, *Adv. Energy Mater.* **2013**, *3*, 1186.
[39] a) X. Yu, Y. Lyu, L. Gu, H. Wu, S.-M. Bak, Y. Zhou, K. Amine, S. N. Ehrlich, H. Li, K.-W. Nam, X.-Q. Yang, *Adv. Energy Mater.* **2014**, *4*, 1300950; b) X. Yu, H. Pan, W. Wan, C. Ma, J. Bai, Q. Meng, S. N. Ehrlich, Y.-S. Hu, X. Q. Yang, *Nano Lett.* **2013**, *13*, 4721.
[40] a) F. Cosandey, D. Su, M. Sina, N. Pereira, G. G. Amatucci, *Micron* **2012**, *43*, 22; b) X. Lu, L. Zhao, X. Q. He, R. J. Xiao, L. Gu, Y.-S. Hu, H. Li, Z. X. Wang, X. F. Duan, L. Q. Chen, J. Maier, Y. Ikuhara, *Adv. Mater.* **2012**, *24*, 3233; c) X. Lu, Y. Sun, Z. L. Jian, X. Q. He, L. Gu, Y.-S. Hu, H. Li, Z. X. Wang, X. F. Duan, L. Q. Chen, J. Maier, Y. Ikuhara, *Nano Lett.* **2012**, *12*, 6192.
[41] D. Su, F. Wang, C. Ma, N. Jiang, *Nano Energy* **2013**, *2*, 343.